Research Article

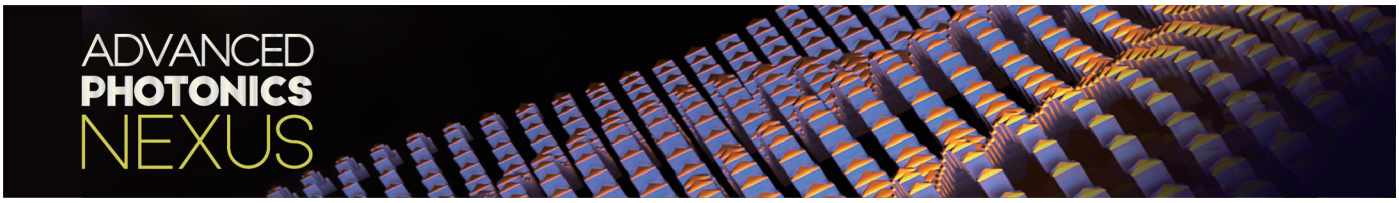

Simultaneous sorting of arbitrary vector structured beams with spin-multiplexed diffractive metasurfaces

Xiaoxin Li,[a] Rui Feng,[a,*] Fangkui Sun,[a,*] Yanxia Zhang,[a] Qi Jia,[a] Donghua Tang,[b] Bojian Shi,[a] Hang Li,[a] Yanyu Gao,[a] Wenya Gao,[a] Yongyin Cao,[a] and Weiqiang Ding[a,c,*]

[a]Harbin Institute of Technology, Institute of Advanced Photonics, School of Physics, Harbin, China
[b]Northeast Forestry University, School of Science, Department of Physics, Harbin, China
[c]Shanxi University, Collaborative Innovation Center of Extreme Optics, Taiyuan, China

Abstract. Vector structured beams (VSBs) offer infinite eigenstates and open up new possibilities for high-capacity optical and quantum communications by the multiplexing of the states. Therefore, the sorting and measuring of VSBs are extremely important. However, the efficient manipulations of a large number of VSBs have simultaneously remained challenging up to now, especially in integrated optical systems. Here, we propose a compact spin-multiplexed diffractive metasurface capable of continuously sorting and detecting arbitrary VSBs through spatial intensity separation. By introducing a diffractive optical neural network with cascaded metasurface systems, we demonstrate arbitrary VSBs sorters that can simultaneously identify Laguerre–Gaussian modes ($l = -4$ to 4, $p = 1$ to 4), Hermitian–Gaussian modes ($m = 1$ to 4, $n = 1$ to 3), and Bessel–Gaussian modes ($l = 1$ to 12). Such a sorter for arbitrary VSBs could revolutionize applications in integrated and high-dimensional optical communication systems.

Keywords: vector structured beams; diffractive optical neural networks; mode sorting; polarization-multiplexed metasurfaces.

Received Feb. 1, 2024; revised manuscript received Apr. 10, 2024; accepted for publication Apr. 26, 2024; published online May 20, 2024.

[DOI: 10.1117/1.APN.3.3.036010]

1 Introduction

Light is endowed with multiple inherent degrees of freedom (DoFs), including spatial intensity, phase, and polarization. Except for prior investigations predominantly focused on spatially uniform polarization states, such as linear and circular polarization, vector structured beams (VSBs) have also been generated by adjusting the nonuniform polarization distribution in the wavefront and transverse planes.[1–5] This enhanced polarization versatility offers significant advantages compared to scalar light in a variety of applications, such as particle trapping, enhanced metrology, and quantum communications.[6–10]

Despite the promising potential of VSBs, numerous questions persist regarding mode sorting and detection. The most popular approaches for detecting VSBs utilize Stokes measurements to determine the polarization state at each point of the beam,[11–13] requiring intricate optics and precise alignment. In addition, the methods for validating VSBs by separating polarization and spatial modes have also been widely adopted.[14,15] However, these methods are only effective for specific spatial modes, resulting in limited pattern diversity. To date, a comprehensive mode detection framework for VSBs that can extrapolate to arbitrary basis vectors is still lacking.

In recent years, optical neural networks have emerged as a disruptive technology, harnessing advantages such as high information capacity, light-speed processing, and massive parallelism.[16–19] The diffractive neural network (DNN), featuring cascaded diffraction layers, has garnered considerable attention for its robust light-field information processing capabilities.[18,20–23] Recent studies have showcased the proficiency of DNN in recognizing scalar structured beams with an arbitrary basis.[20,24,25] Specifically, mode (de)multiplexers scalable for hundreds of optical modes have been demonstrated using spatial light modulators (SLMs) and

*Address all correspondence to Rui Feng, fengrui_0223@163.com; Fangkui Sun, fksun@hit.edu.cn; Weiqiang Ding, wqding@hit.edu.cn

multiple mirrors.[26] In addition, a diffractive optical neural network tailored for low crosstalk orbital angular momentum (OAM) multiplexing/demultiplexing has also been developed.[27]

Despite the successes, however, their processing scope is confined to scalar structured beams. This limitation arises from the common use of polarization-independent phase plates or SLMs as phase masks, which lack the capability to manipulate arbitrary vector light fields. Achieving independent operation of dual orthogonal polarization bases typically requires a polarization beam-splitting scheme, introducing additional complexity and bulk. Therefore, the pursuit of a compact device capable of directly processing and identifying VSBs with arbitrary bases holds significant appeal for diverse applications.

In this work, we present a groundbreaking optical neural network utilizing spin-multiplexed diffractive metasurfaces for simultaneous classification of arbitrary VSBs. Leveraging the exceptional polarization control capabilities of optical metasurfaces, we offer an efficient solution for the conversion and sorting of VSBs. To illustrate this concept, a four-layer spin-multiplexed diffractive metasurface is employed to process VSBs composed of Laguerre–Gaussian (LG) beams with azimuthal indices ranging from $l = -4$ to $+4$ and radial indices ranging from $p = 0$ to 3. The focus position in the output plane is determined through a straightforward comparison search to ascertain the modes of the input VSBs. More importantly, we also successfully identify hybrid VSBs formed by multiple spatial basis, including LG, Hermitian–Gaussian (HG), and Bessel–Gaussian (BG) beams. The outcomes validate the robust capability of multiple diffractive metasurfaces in classifying and identifying VSBs. This method is efficient and offers a rapid, straightforward, and compact solution for hybrid VSB identification in diverse applications such as quantum entangled state detection and high-throughput optical communications.

2 Principle of Multiplexed Diffractive Metasurface Design

2.1 Working Principle of Simultaneous Sorting of VSBs

Figure 1 schematically shows the mode detection framework utilizing spin-multiplexed diffractive metasurfaces. First, let us examine the determination of mode indices in VSBs. In theoretical terms, a vectorial structured light field can be represented through the following unnormalized expression:[5]

$$|\psi\rangle = |s_1\rangle|p_1\rangle + |s_2\rangle|p_2\rangle, \tag{1}$$

where $|p_{1,2}\rangle$ denotes the polarization DoFs, corresponding to a pair of orthogonal polarization bases, such as left-handed circular polarization (LCP) and right-handed circular polarization (RCP). $|s_{1,2}\rangle$ represents the spatial DoFs, typically involving structured beams with high-order mode indices, such as LG and HG beams. VSBs are conceptualized as a linear superposition of the orthogonal circularly polarized bases carrying various structured beam modes, as shown in Fig. 1(a). Consequently, for comprehensive detection of VSBs, it is essential to independently detect all mode indices conveyed by these two orthogonal polarizations.

As a typical type of optical neural network, DNN has demonstrated effectiveness in manipulating complex light fields through linear transformations. By precisely adjusting the phase in the hidden layer, DNN can convert the input light field into predefined Gaussian spots across different regions, thus

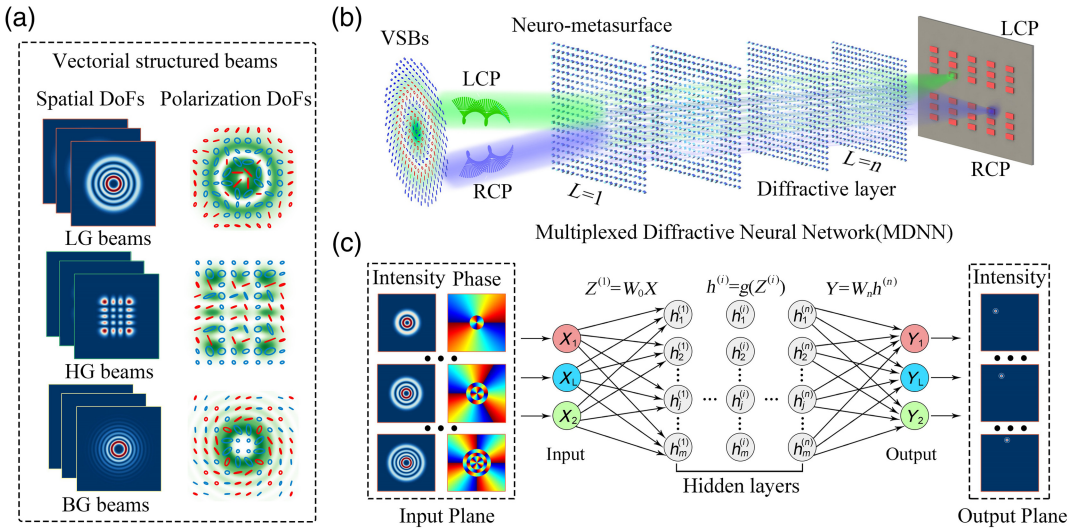

Fig. 1 Schematic and working mechanism of VSB sorting enabled by spin-multiplexed diffractive metasurfaces. (a) The VSBs exhibit polarization DoFs and spatial DoFs with LG beams, HG beams, and BG beams (including arbitrary superpositions of them). The red line denotes the LCP component, while the blue line signifies the RCP component. (b) Schematic diagram of VSBs sorting based on spin-multiplexed diffractive metasurfaces. The input is a VSB composed of an LG beam, the hidden layer is composed of multilayer spin-multiplexed metasurfaces acting as neurons, and the output is a focused Gaussian bright spot in the planar detection area. (c) The architecture of the DNN. Phase and intensity information of the incident light is processed through several hidden layers and then optimized by an error backpropagation algorithm.

facilitating pattern classification. This capability presents a valuable approach for the detection and characterization of high-order VSBs.

To fully identify the mode indices of VSBs, we introduce a spin-multiplexed metasurface that independently processes two orthogonal circularly polarized waves, creating two distinct output sets, as shown in Fig. 1(b). By examining the spot position on the output plane, we can determine all mode parameters of the incident light, enabling a comprehensive classification of VSBs with a single measurement.

We set the spatial DoFs of an LG beam to be the azimuthal index l and radial index p. The VSBs can be written in the following form:

$$|\psi\rangle = \frac{1}{\sqrt{2}}|\mathrm{LG}_{l_L,p_L}\rangle|\sigma_+\rangle + \frac{1}{\sqrt{2}}|\mathrm{LG}_{l_R,p_R}\rangle|\sigma_-\rangle, \tag{2}$$

where $|\mathrm{LG}_{l_L,p_L}\rangle$ and $|\mathrm{LG}_{l_R,p_R}\rangle$ are LG beams, and $|\sigma_\pm\rangle$ represents the RCP and LCP states, respectively. An LG beam propagating along the z direction can be expressed as

$$\begin{aligned}\mathrm{LG}_{l,p} = &\sqrt{\frac{2p!}{\pi(p+|l|)!}}\frac{1}{w(z)}\left[\frac{\sqrt{2}r}{w(z)}\right]^{|l|}\exp\left[\frac{-r^2}{w^2(z)}\right]L_p^{|l|}\left[\frac{2r^2}{w^2(z)}\right]\\ &\times\exp(il\varphi)\exp\left[\frac{ikr^2z}{2(z^2+z_R^2)}\right]\\ &\times\exp\left[-i(2p+|l|+1)\tan^{-1}\left(\frac{z}{z_R}\right)\right],\end{aligned} \tag{3}$$

where $w(z)$ denotes the beam radius and z_R is the Rayleigh length. The LG beam serves as an input to the DNN, and the output manifests as the fundamental Gaussian beam mode at diverse spatial locations, as shown in Fig. 1(c).

Optimization of the hidden-layer metasurfaces enables gradual manipulation of the incident light field to yield the targeted light field. As a result, accurate identification of VSBs can be accomplished by discerning the spatial position of the focus within the detection zone. For LCP/RCP waves, the focus is assigned within the upper/lower half of the output plane. This methodology has facilitated the detection of spin angular momentum. Importantly, this framework can equally be applied to VSBs composed of BG beams and HG beams.

2.2 Design of Spin-Multiplexed Metasurfaces

Figure 2(a) shows the schematic diagram of the spin-multiplexed metasurface. The metasurface unit consists of rectangular TiO_2 nanopillars on a quartz substrate. The nanopillars have a uniform height H, whereas their in-plane dimensions (D_x, D_y) and orientation angle (θ) vary spatially. The finite-difference time-domain (FDTD) algorithm was employed to conduct full-wave simulations to scrutinize the transmission attributes of the TiO_2 nanopillars. The height H of the nanopillars was set to 600 nm to achieve the desired 2π phase coverage. The lattice constant was selected as 450 nm to comply with the Nyquist sampling law. Figures 2(b) and 2(c) show the simulated phase shift and transmission of x- and y-polarized lights from a nanopillar at the wavelength of $\lambda_0 = 532$ nm as a function of diameter (D_x, D_y). Based on the simulation results, we selected a set of 16 nanopillars to provide 16 orders of phase levels covering 2π range for φ_x and φ_y. The phase and polarization conversion efficiencies (PCEs) of the nanopillars are shown in Fig. 2(d).

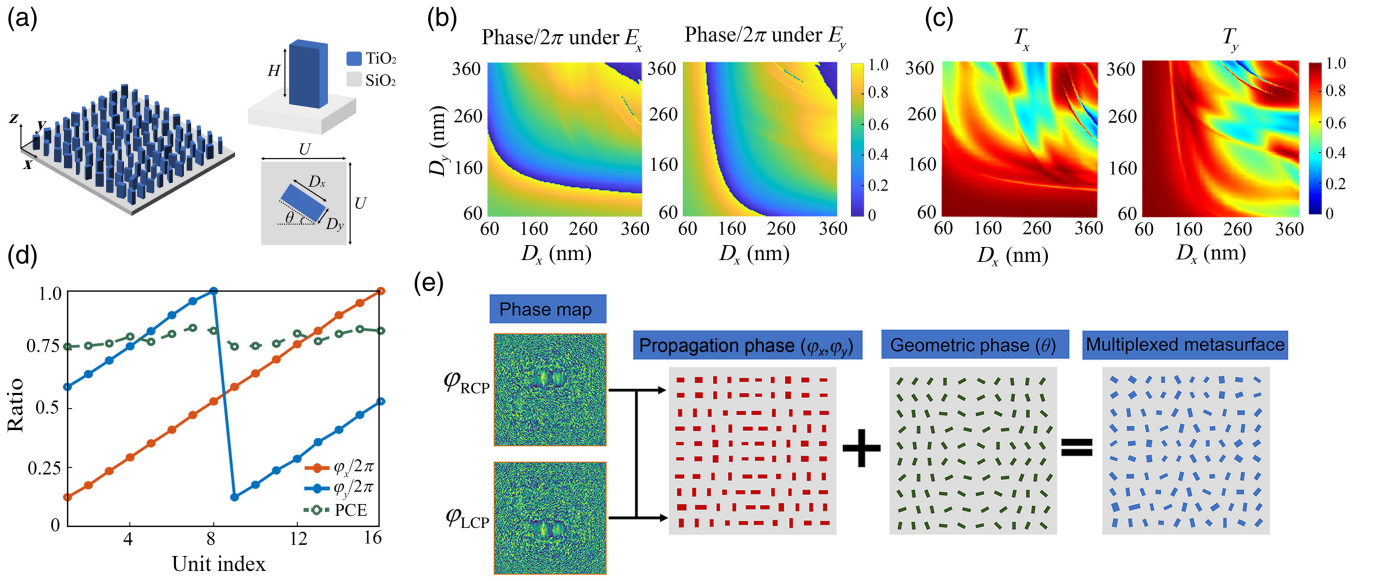

Fig. 2 Structure design of a spin-multiplexed metasurface. (a) Left, schematic of a metasurface composed of TiO_2 nanopillars. Right, perspective view and top view of the unit cell placed on a quartz substrate. The incident wavelength is 532 nm, the nanopillar period is $U = 400$ nm, and the height is $H = 600$ nm. (b) and (c) Phase shifts and transmission under x-polarized light and y-polarized light, respectively. (d) Phase delay and PCE of the selected 16 nanopillars. (e) Design method for generating arbitrary spin-multiplexed metasurfaces. Given two arbitrary phase maps $(\varphi_{RCP}, \varphi_{LCP})$, the propagation phase (φ_x, φ_y) and the geometric phase θ of the metasurface pixels are calculated to design the in-plane sizes and rotation angles.

It is crucial to note that metasurfaces induce not only phase modulation but also amplitude crosstalk. Consequently, through parameter optimization, we make the PCE of the nanopillar basically consistent at the 532 nm wavelength, eliminating the influence of amplitude as much as possible while maintaining high efficiency (PCE > 0.75). The overall design process of the metasurface is shown in Fig. 2(e). By combining the geometric phase and the propagation phase (see Section I of Supplementary Material for detailed derivation), the in-plane size (D_x, D_y) and spatial direction angle (θ) of the nanopillar are determined at all the positions.

2.3 Training of Spin-Multiplexed Diffractive Metasurfaces

To elucidate the spatial phase distribution of multilayer metasurfaces, we train a DNN. Here, we consider that each layer contains 200 × 200 units, and thus the number of neurons reaches 40,000 on each layer, providing ample DoFs for the manipulation of the light field. The wavelength is fixed at $\lambda = 532$ nm, and the spacing between the foremost and rearmost layers is set to be 75 times the wavelength (75λ), facilitating efficient field information transmission from the initial layer to each neuron.

Figure 3(a) shows a typical diffraction process. Throughout the training phase, the phase of each unit is treated as a learnable parameter of the network, and an error backpropagation algorithm is implemented for iterative refinement. See Supplementary Material, Section II for more details about the error backpropagation algorithm. It is evident that an increase in the number of hidden layers results in a decrease in crosstalk, which is defined as

$$\text{Crosstalk} = 10 \times \lg\left(\frac{I^N_{\text{ALL}/i}}{I^S_{\text{ALL}}}\right), \tag{4}$$

where I^S_{ALL} is the signal energy fraction when i'th channel is on, and $I^N_{\text{ALL}/i}$ is the noise energy fraction. Figure 3(b) shows the average crosstalk at varying numbers of hidden layers in the identification of diverse modes. With the increase of hidden layers, the average crosstalk exhibits a gradual decrease. Here, four hidden layers are chosen because an increase in the number of hidden layers correlates with a higher transmission loss, since the transmittance of a single metasurface approximates 75%. The crosstalk at this juncture closely resembles the performance of commercial mode sorters. In addition, an increase in mode numbers leads to greater crosstalk, thus rendering the selection of three hidden layers unsuitable. Figure 3(c) presents the results of scalar diffraction calculations of $\text{LG}_{l=-4,p=3}$ and $\text{LG}_{l=-3,p=2}$. The Gaussian spot corresponding to the LCP incident light materializes in the corresponding region on the output plane, and a parallel occurrence is observed with the RCP light. Figure 3(d) shows the computed energy distributions of 36 modes. The outcomes suggest that the trained model possesses the competence to accurately identify all VSBs.

3 Results and Discussion

3.1 Simultaneous Sorting of High-Order VSBs

To assess the viability of spin-multiplexed diffractive metasurfaces for detecting VSBs, we focus on high-order vector vortex beams (HOVVBs); the results are shown in Fig. 4. The spatial DoFs for the HOVVB are represented by an LG beam with

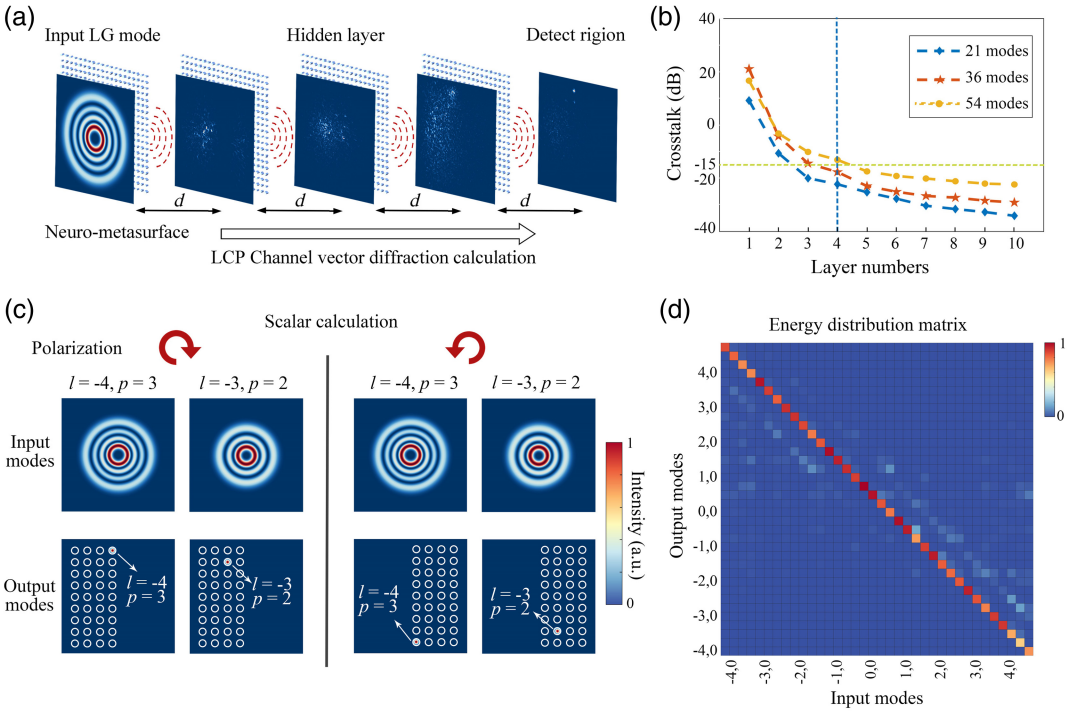

Fig. 3 Training of diffractive metasurface for pattern detection. (a) Flowcharts of vector diffraction calculation simulation. (b) Identifying the crosstalk of mode numbers as a function of different numbers of hidden layers. (c) Scalar diffraction calculation results for incident mode identification. (d) Energy distribution matrix results of 36 modes (see the text for details on the modes).

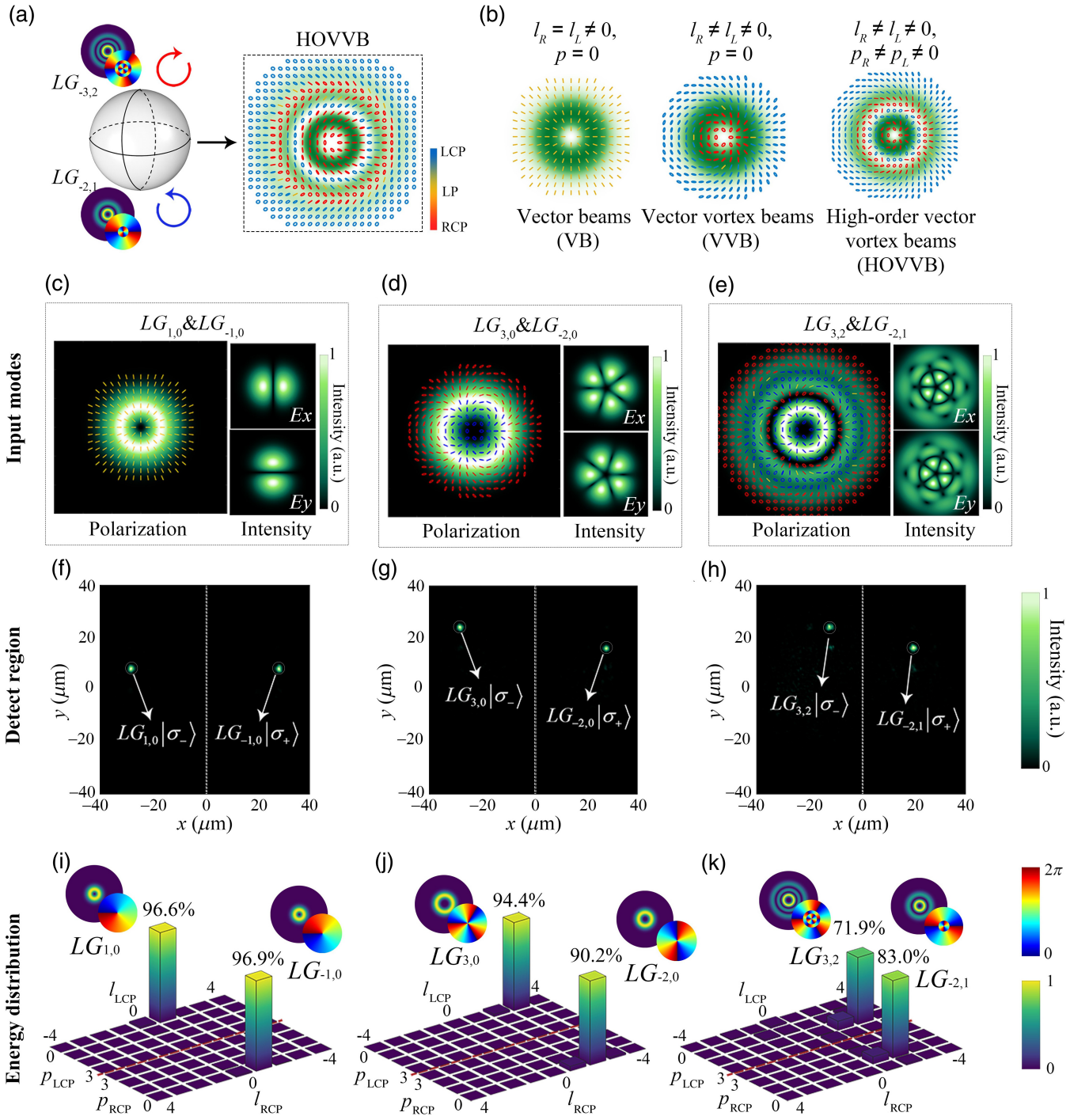

Fig. 4 Characterization of spin-multiplexed diffractive metasurfaces for identifying high-order VSBs. (a) Poincaré sphere representation of HOVVBs. (b) Intensity patterns of three typical VSBs. The red line denotes the LCP component, the blue line signifies the RCP component, and the yellow line represents the linearly polarized (LP) component. (c)–(e) The polarization distributions and intensity patterns of the input light fields, and the intensities of E_x and E_y components. (f)–(h) Measured intensity distribution of the output plane. (i)–(k) The normalized energy ratio of 72 output channels.

angular index l and radial index p, as shown in Fig. 4(a). Figure 4(b) displays HOVVBs, cylindrical vector beams (VBs), and vector vortex beams (VVBs).[1,28–32] In this configuration, the angular index l and radial index p serve as the classification keys. Therefore, the pattern detection of HOVVBs exhibits enhanced adaptability and versatility. With our current knowledge, a stable scheme for detecting the full range of modes of HOVVB remains elusive.

Here, we employ vector diffraction to validate the functionality of the proposed neural metasurface. Figures 4(c)–4(k) show the results of the input vector light fields $\psi_1 = (|\mathrm{LG}_{1,0}\rangle|\sigma_+\rangle + |\mathrm{LG}_{-1,0}\rangle|\sigma_-\rangle)/\sqrt{2}$, $\psi_2 = (|\mathrm{LG}_{3,0}\rangle|\sigma_+\rangle + |\mathrm{LG}_{-2,0}\rangle|\sigma_-\rangle)/\sqrt{2}$, and $\psi_3 = |\mathrm{LG}_{3,2}\rangle|\sigma_+\rangle + |\mathrm{LG}_{-2,1}\rangle|\sigma_-\rangle/\sqrt{2}$. See Supplementary Material, Section III for more detailed results of the input vector fields. For vector simulation, the phase distribution is converted into the corresponding structural parameters of the metasurface. Subsequently, the near field is obtained through FDTD simulation, followed by the extrapolation to the far field. Upon completing the calculation of the last layer, the output light intensity distribution is obtained.

The spin-multiplexed diffractive metasurfaces are trained based on four hidden layers and achieve convergence after 500 iterations. Figures 4(c)–4(e) show the intensity and polarization distribution of the input light field, along with the corresponding electric field components of E_x and E_y. Figures 4(f)–4(h) showcase the light-intensity distribution within the detection area, revealing two distinct Gaussian bright spots on the output plane, from which we can accurately identify the spatial pattern of the incident light field. The complete diffraction efficiency of the four-layer metasurface stands at 15.3%, which can be attributed to the inherent loss of the metasurface and the energy dissipation throughout the diffraction process. Further enhancement of efficiency can be attained through the optimization of the metasurface units. Therefore, with a single measurement, such a metadevice can fully resolve all modes of HOVVBs, encompassing spin angular momentum (s), angular quantum number (l), and radial quantum number (p).

Finally, we calculated the normalized energy ratio of the output channels to evaluate the crosstalk, with the results presented in Figs. 4(i)–4(k). The inset depicts the intensity and phase distribution of the LCP and RCP components of the incident light. It is evident that the energy peak accurately aligns with the corresponding mode position, and its proportion exceeds 70% even with the consideration of the radial index p.

3.2 Simultaneous Sorting of Superimposed VSBs

For further demonstration, we then investigate the recognition of arbitrary VSBs, as shown in Fig. 5. We use three typical structural beam modes to compose very complex DoFs. Among them, the mode indices of the LG beam are $l = -2, -1, 1, 2$ and $p = 1, 2, 3$. The mode indices of the HG beams are $m = 1, 2, 3, 4$ and $n = 1, 2, 3$. The topological charge of

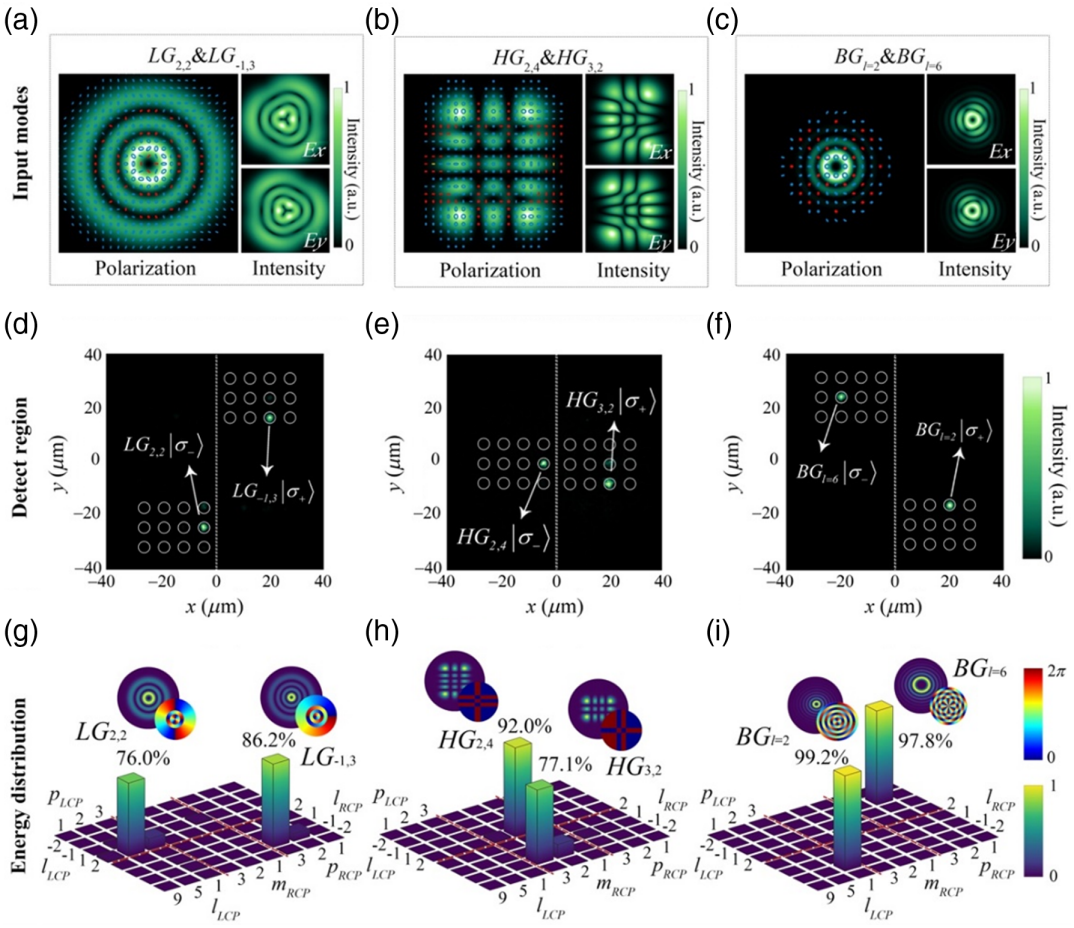

Fig. 5 Characterization of spin-multiplexed diffractive metasurfaces for identifying arbitrary VSBs. (a)–(c) The polarization distributions and intensity profiles of the input light fields, and the intensity results of the E_x and E_y components. (d)–(f) Measured intensity distribution of the output plane. (g)–(i) The normalized energy ratio of 72 output channels.

the BG beam of $l = 1, 2, \ldots, 12$ is selected. Employing all 36 modes as the input, the output of spin-multiplexed diffractive metasurfaces consistently remained a Gaussian light spot at the predetermined position. This approach uniquely enables the identification of arbitrary vectorial structured beams in a single detection, which was unachievable with prior methods.

We then evaluated the performance of the components through vector components. To demonstrate its capabilities, we select three vector modes of $\psi_1 = (|\mathrm{LG}_{2,2}\rangle|\sigma_+\rangle + |\mathrm{LG}_{-1,3}\rangle|\sigma_-\rangle)/\sqrt{2}$, $\psi_2 = (|\mathrm{HG}_{3,2}\rangle|\sigma_+\rangle + |\mathrm{HG}_{2,4}\rangle|\sigma_-\rangle)/\sqrt{2}$, and $\psi_3 = (|\mathrm{BG}_2\rangle|\sigma_+\rangle + |\mathrm{BG}_6\rangle|\sigma_-\rangle)/\sqrt{2}$. See Supplementary Material, Section IV for more details. Figures 5(a)–5(c) show the patterns of input VSBs, characterized by distinct polarization distributions and field intensity patterns. These beams propagate through multilayer neural metasurfaces and generate varied light spots on the output plane, as shown in Figs. 5(d)–5(f). The figures show the light-intensity distribution in the detection area as two distinct Gaussian spots on the output plane. Furthermore, the normalized energy ratio of the output channels is quantified to assess the crosstalk, as shown in Figs. 5(i)–5(k). These outcomes confirm the precise recognition of the input light fields. Simultaneously, the method demonstrates the classification and identification of multiple groups of nonorthogonal vector beams, a task previously deemed unattainable by existing methodologies.

In addition, we consider the experimental feasibility of the proposed four-layer multiplexed diffractive metasurface. The TiO_2 metasurfaces can be fabricated using standard nanofabrication processes with a combined process of electron-beam lithography and reactive ion etching. Further, to align cascaded metasurfaces accurately, a high-precision six-dimensional displacement stage and a high-resolution microscope can be employed for optimal alignment.[23] In addition, photoresist can serve as a spacer layer for preparing multilayer integrated cascade metasurfaces. This approach achieves layer-to-layer alignment during the fabrication process; thus the monolithic diffractive metasurface eliminates the need for subsequent manual alignment.

4 Conclusion

In summary, we have proposed a spin-multiplexed diffractive metasurface method for simultaneous mode sorting of VSBs with arbitrary complex spatial and polarization distributions. This approach enables the simultaneous acquisition of the complete patterns in a single detection, without any other additional processing used in previous investigations. We investigated two detection modes: high-order VSBs (spatial DoFs of LG beams with $l = -4$ to 4 and $p = 0$ to 3) and superimposed VSBs (spatial DoFs being the superposition of LG, HG, and BG beams) and successfully demonstrated the effectiveness of our new method. Notably, this technique can be extended to encompass vector beams with any orthogonal basis set, including single vector families and hybrid vector families. Due to the current lack of nonlinear components in diffractive networks, the sorter is unable to distinguish vector modes with different relative phases, which will be considered in future work. In addition, mapping the vector onto a single spot will further reduce the energy consumption of the sensor, which remains an open challenge. In short, our proposed scheme offers significant advantages in system integration and miniaturization due to the flatness and compactness of the metasurface. The potential of this technology spans a broad spectrum of applications, including high-capacity optical communications and quantum information processing.

Code and Data Availability

The simulated data that support this work are available from the corresponding authors upon reasonable request.

Acknowledgments

This work was supported by the National Natural Science Foundation of China (Grant No. 12274105), the Heilongjiang Natural Science Funds for Distinguished Young Scholars (Grant No. JQ2022A001), the Fundamental Research Funds for the Central Universities (Grant No. HIT.OCEF.2021020), and the Joint Guidance Project of the Natural Science Foundation of Heilongjiang Province (Grant No. LH2023A006).

References

1. Q. Zhan, "Cylindrical vector beams: from mathematical concepts to applications," *Adv. Opt. Photonics* **1**(1), 1–57 (2009).
2. X.-L. Wang et al., "Optical orbital angular momentum from the curl of polarization," *Phys. Rev. Lett.* **105**(25), 253602 (2010).
3. J. Chen, C. Wan, and Q. Zhan, "Vectorial optical fields: recent advances and future prospects," *Sci. Bull.* **63**(1), 54–74 (2018).
4. C. He, Y. Shen, and A. Forbes, "Towards higher-dimensional structured light," *Light Sci. Appl.* **11**(1), 205 (2022).
5. I. Nape et al., "Revealing the invariance of vectorial structured light in complex media," *Nat. Photonics* **16**, 538–546 (2022).
6. W. Ding et al., "Photonic tractor beams: a review," *Adv. Photonics* **1**(2), 024001 (2019).
7. Y. Yang et al., "Optical trapping with structured light: a review," *Adv. Photonics* **3**(3), 034001 (2021).
8. H. Rubinsztein-Dunlop et al., "Roadmap on structured light," *J. Opt.* **19**(1), 013001 (2016).
9. L. Fang et al., "Vectorial Doppler metrology," *Nat. Commun.* **12**(1), 4186 (2021).
10. M. Erhard, M. Krenn, and A. Zeilinger, "Advances in high-dimensional quantum entanglement," *Nat. Rev. Phys.* **2**(7), 365–381 (2020).
11. J. Yao et al., "Quantitative detection of high-order Poincaré sphere beams and their polarization evolution," *Opt. Express* **31**(2), 3017–3027 (2023).
12. S. N. Khan et al., "Detection of partially coherent polarization singular vector beams using Stokes polarimetry," *Appl. Phys. Lett.* **118**(5), 051104 (2021).
13. M. McLaren, T. Konrad, and A. Forbes, "Measuring the nonseparability of vector vortex beams," *Phys. Rev. A* **92**(2), 023833 (2015).
14. C. Rosales-Guzmán, B. Ndagano, and A. Forbes, "A review of complex vector light fields and their applications," *J. Opt.* **20**(12), 123001 (2018).
15. Y. Guo et al., "Spin-decoupled metasurface for simultaneous detection of spin and orbital angular momenta via momentum transformation," *Light Sci. Appl.* **10**(1), 63 (2021).
16. J. Liu et al., "Research progress in optical neural networks: theory, applications and developments," *PhotoniX* **2**(1), 5 (2021).
17. F. Ashtiani, A. J. Geers, and F. Aflatouni, "An on-chip photonic deep neural network for image classification," *Nature* **606**(7914), 501–506 (2022).
18. X. Lin et al., "All-optical machine learning using diffractive deep neural networks," *Science* **361**(6406), 1004–1008 (2018).
19. B. Dong et al., "Higher-dimensional processing using a photonic tensor core with continuous-time data," *Nat. Photonics* **17**(12), 1080–1088 (2023).

20. Z. Huang et al., "All-optical signal processing of vortex beams with diffractive deep neural networks," *Phys. Rev. Appl.* **15**(1), 014037 (2021).
21. X. Luo et al., "Metasurface-enabled on-chip multiplexed diffractive neural networks in the visible," *Light Sci. Appl.* **11**(1), 158 (2022).
22. C. He et al., "Pluggable multitask diffractive neural networks based on cascaded metasurfaces," *Opto-Electron. Adv.* **7**, 230005 (2024).
23. F. Mei et al., "Cascaded metasurfaces for high-purity vortex generation," *Nat. Commun.* **14**(1), 6410 (2023).
24. Q. Jia et al., "Universal translation operator for Laguerre–Gaussian mode sorting," *Appl. Phys. Lett.* **121**(19), 191104 (2022).
25. Q. Jia et al., "Compensating the distorted OAM beams with near zero time delay," *Appl. Phys. Lett.* **121**(1), 011104 (2022).
26. N. K. Fontaine et al., "Laguerre-Gaussian mode sorter," *Nat. Commun.* **10**(1), 1865 (2019).
27. Z. Liu et al., "Broadband, low-crosstalk, and massive-channels OAM modes de/multiplexing based on optical diffraction neural network," *Laser Photonics Rev.* **17**(4), 2200536 (2023).
28. G. Milione et al., "Higher-order Poincare sphere, Stokes parameters, and the angular momentum of light," *Phys. Rev. Lett.* **107**(5), 053601 (2011).
29. T. Giordani et al., "Machine learning-based classification of vector vortex beams," *Phys. Rev. Lett.* **124**(16), 160401 (2020).
30. J. Ni and C.-W. Qiu, "A minimalist single-layer metasurface for arbitrary and full control of vector vortex beams," *Adv. Mater.* **32**(6), 1905659 (2020).
31. D. Yang et al., "Multiwavelength high-order optical vortex detection and demultiplexing coding using a metasurface," *Adv. Photonics Nexus* **1**(1), 016005 (2022).
32. L. Li et al., "Photon total angular momentum manipulation," *Adv. Photonics* **5**(5), 056002 (2023).

Xiaoxin Li is a doctoral candidate at the School of Physics, Harbin Institute of Technology. He received his bachelor's degree from Harbin Institute of Technology in 2019 and his master's degree in physics from the same institution in 2021. His principal research areas encompass metasurface optical computing, diffractive neural networks, polarization imaging, and spectral imaging with metalens.

Rui Feng received his PhD from Harbin Institute of Technology in 2015. He is an assistant professor at the School of Physics of Harbin Institute of Technology (HIT). Before joining HIT in 2017, he was a research fellow at the National University of Singapore. His current research focuses on optical metasurfaces, nearly perfect absorber, and optical field manipulation.

Fangkui Sun is an associate professor at the School of Physics, Harbin Institute of Technology. His primary research interests encompass micro-nano optoelectronic devices, photonic chips, semiconductor devices, and metasurfaces.

Weiqiang Ding is a professor and doctoral supervisor at the School of Physics, Harbin Institute of Technology and a recipient of the Heilongjiang Provincial Outstanding Youth Fund. His research focuses on optical metasurfaces, photonic crystals, light field control, photonic chips, and optical manipulation. He has published more than 100 peer-reviewed journal papers in Nature Photonics, Physical Review Letters, Advanced Photonics, and Light: Science & Applications etc.

Biographies of the other authors are not available.